Controlled Diffusion airfoil self-noise, an acoustic far-field prediction

Andrea Arroyo Ramo, Stéphane Moreau, Richard Sandberg, Michaël Bauerheim, Marc Jacob

Controlled Diffusion airfoil self-noise, an acoustic far-field prediction

Andrea Arroyo Ramo*
Université de Sherbrooke, Sherbrooke, Quebéc, J1K2R1, Canada

Stéphane Moreau†
Université de Sherbrooke, Sherbrooke, Quebéc, J1K2R1, Canada

Richard D. Sandberg‡
The University of Melbourne, Melbourne, 3010, Australia

Michaël Bauerheim§
ISAE-SUPAERO, Université de Toulouse, 31400 Toulouse, France

Marc C. Jacob¶
Ecole Centrale de Lyon, Université de Lyon, 69130 Ecully, France

Direct Numerical Simulations (DNS) of the compressible flow over a Controlled Diffusion (CD) airfoil are conducted. The computations are coupled to an acoustic solver based on the Ffowcs Williams & Hawkings formulation to obtain far field noise predictions. The objective of this work is to investigate the turbulent flow field and the associated noise generation mechanisms at the vicinity of the trailing edge. The installation effects are included in the computations by introducing non-uniform boundary conditions computed by a precursor RANS calculation. Three noise sources have been found, the flow separation and reattachment, the interaction between the attached turbulent flow and the trailing edge and a secondary instability in the near wake.

Keywords: CFD · DNS · Aeroacoustics · Airfoil noise

I. Introduction

Noise pollution is a general concern as it affects both human and animal health. In particular, airfoil noise is an important contributor to both the total and broadband noise emitted by turbomachinery applications. For rotating machines such as engine cooling fans and wind turbine propellers, the blade self-noise is responsible of the minimum noise level produced, and it is due to the interaction between the eddies of the turbulent boundary layer (BL) and wake with the airfoil itself. At the trailing edge, the distortion of these eddies that are convected along the airfoil converts the vorticity modes into acoustic waves. This trailing-edge noise can become the dominant noise source in a rotating machine. In the present study, the broadband noise generated by the interaction of the turbulent flow with the trailing edge is addressed.

In order to study trailing-edge noise, several approaches have been introduced over time, from analytical models to computational simulations, including experimental campaigns. A variety of approaches have been proposed to model trailing-edge noise, most of them based on the studies of Ffowcs Williams & Hall [1], Amiet [2] and Howe [3]. These approaches rely on modelling the airfoil as a flat plate, ignoring the airfoil chord, thickness, and curvature. Extensions to these formulations have been developed to include the leading-edge scattering and finite geometry.

In the last decade, high-fidelity simulations (Large Eddy Simulations – LES – [4],[5],[6], and Direct Numerical Simulations –DNS– [7–13]) have been used to perform predictions of trailing-edge noise. These simulations are

*PhD candidate, Département Aérodynamique, Énergétique et Propulsion, ISAE-Supaero and Département de Génie Méchanique, Université de Sherbrooke, andrea.arroyo.ramo@usherbrooke.ca

†Professor, Mechanical Engineering Department at Université de Sherbrooke, AIAA Lifetime Member.

‡Professor, Department of Mechanical Engineering at the University of Melbourne, AIAA Lifetime Member.

§Associate Professor, Département Aérodynamique, Énergétique et Propulsion, ISAE-SUPAER0, BP 54032, F-31055 Toulouse Cedex 4.

¶Professor, Université de Lyon, École Centrale de Lyon, INSA Lyon, Université Claude Bernard Lyon I, CNRS, Laboratoire de Mécanique des Fluides et d'Acoustique, UMR 5509, F-69134 Ecully Cedex, France, AIAA Member.

usually coupled with an acoustic analogy to propagate the acoustics from the resolved near field towards the far field. High-fidelity simulations have shown that not only the trailing-edge noise is the main source of noise. Sandberg *et al.* [8] observed that the region where transition occurs and the flow is reattached on the suction side becomes a noise source region. Jones *et al.* [14] concluded that the trailing-edge noise contributes mainly to the low frequencies, whereas most of the high-frequency contribution comes from the transition/reattachment region. Therefore, even though the trailing edge can be considered as the main noise source, other contributors to airfoil self noise exist.

The objective of the work presented herein is to investigate the turbulent flow field and the contribution of the different noise sources on the airfoil, focusing on the broadband noise generation in the vicinity of the trailing edge. The investigation is carried out on the Controlled Diffusion (CD) airfoil [15][16], which is a cambered airfoil used in the industrial applications such as turbo-engine compressor and fan blades, and automotive engine cooling fans. This airfoil is capable of controlling the flow and losses around its surface by preventing an excessive boundary layer growth. The CD airfoil under study has a 4% thickness-to-chord ratio and a camber angle of 12°. Although recent investigations explored Mach numbers up to transonic regime [4], past studies of this airfoil have been mainly dedicated to low Reynolds number DNS' at low Mach numbers [17],[18]. This study follows the previous work of Arroyo *et al.* [19], where the airfoil is first immersed in the flow at a geometric angle of attack of 8°, a Reynolds number of 1.5×10^5 and a Mach number of 0.25. The focus was then only on the mean aerodynamic flow and the prediction of wall-pressure spectra.

To validate the numerical results, the simulations must be compared to equivalent experimental conditions [5]. There exist important installation effects occurring in open-jet anechoic wind tunnels, since the airfoil is immersed in the potential core of the jet, which is a non-uniform flow. These installation effects modify both the flow around the airfoil and the sound field [15]. The boundary layer development and flow separation regions are modified [18], as well as the airfoil loading. Therefore, in the DNS of this study, the wind tunnel geometry is included.

II. Numerical modeling

A. Flow-field model

The simulations that are conducted in the present study are 3D DNS of the flow over the CD airfoil at a geometrical angle of attack of 8°. The airfoil is embedded in the potential core of a free-jet wind-tunnel at a free-stream Mach number of $M = 0.25$ and a chord-based Reynolds number of $Re_c = 1.5 \times 10^5$. Once the simulation has been statistically converged, its primitive variables are recorded over 6 flow-through times in the whole domain. To match with experimental conditions, the flow parameters are scaled with a reference velocity $U_0 = 16$ m/s and airfoil chord length $c = 0.1356$ m.

The flow is governed by the full compressible Navier-Stokes equations. These are the continuity, momentum and energy conservation equations (Eq. (1)-(3) respectively) in their non dimensional form. The normalization parameters are the airfoil chord length, and the free-stream velocity, density and temperature.

$$\frac{\partial \rho}{\partial t} + \frac{\partial}{\partial x_j}\left(\rho u_j\right) = 0 \tag{1}$$

$$\frac{\partial}{\partial t}\left(\rho u_i\right) + \frac{\partial}{\partial x_j}\left[\rho u_i u_j + p\delta_{ij} - \tau_{ij}\right] = 0 \tag{2}$$

$$\frac{\partial}{\partial t}(\rho e) + \frac{\partial}{\partial x_j}\left[\rho u_j\left(e + \frac{p}{\rho}\right) + q_j - u_k \tau_{kj}\right] = 0 \tag{3}$$

The total energy e is defined, together with the molecular stress tensor τ_{ij} and heat flux vector q_i as follows:

$$e = \frac{T}{\gamma(\gamma-1)\mathrm{M}^2} + \frac{u_k u_k}{2} \tag{4}$$

$$\tau_{ij} = \frac{\mu}{\mathrm{Re}}\left(\frac{\partial u_i}{\partial x_j} + \frac{\partial u_j}{\partial x_i} - \frac{2}{3}\frac{\partial u_k}{\partial x_k}\delta_{ij}\right) \tag{5}$$

$$q_i = \frac{-1}{(\gamma-1)M^2}\frac{\mu}{RePr}\frac{\partial T}{\partial x_i} \tag{6}$$

where Pr stands for the Prandtl number, which is assumed to be constant ($Pr = 0.72$) and the dynamic viscosity μ is

computed from the dimensionless Sutherland's law. Finally, the non-dimensional state equation

$$p = \frac{\rho T}{\gamma M^2} \tag{7}$$

permits to obtain the pressure to close the system of equations with $\gamma = 1.4$.

1. Numerical solver and grid

The numerical code to perform the simulations is *HiPSTAR* (High Performance Solver for Turbulence and Aeroacoustic Research) [20]. It uses a 4^{th}-order central standard-difference accurate scheme with Carpenter boundary stencils in the x-y (streamwise and cross-stream) directions [21]. In the spanwise direction, a spectral method based on the FFTW3 library is employed. The advantage of *HiPSTAR* is that it uses an ultra low-storage five-stage Runge–Kutta integration scheme, which reduces the storage capacity requirements in the time evolution resolution.

The isolated CD airfoil simulations have been carried out in a reduced rectangular domain (see Fig. 1a) extended 2 chords upstream of the trailing edge and 2.5 chords downstream of the trailing edge. The top and bottom boundaries are located at a distance of 1.5 and 1 chord from the trailing edge, respectively. This reduced domain as it will be further explained in Sec. II.A.2, is meant to fit the airfoil in the jet core with the aim of reproducing free-jet experimental conditions. The computational domain is composed of two overset blocks. Both blocks are structured meshes and are independent of each other and coupled using a stable overset technique [22].

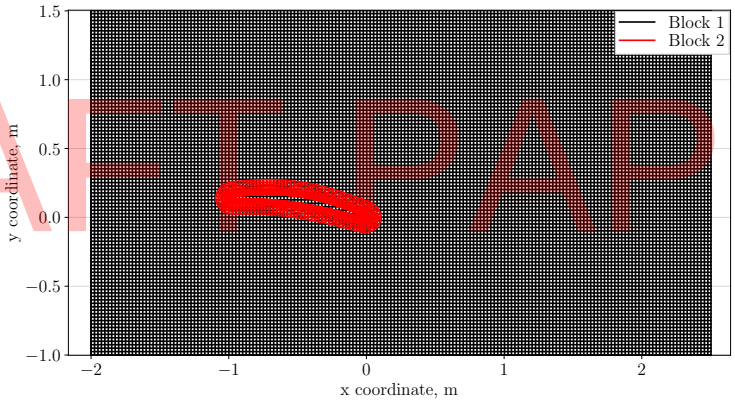

(a) Complete domain meshing. Mesh shown every 10 gridlines to enhance visualisation.

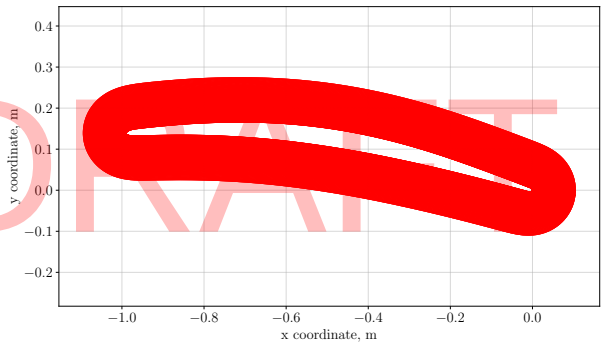

(b) O-grid meshing detail.

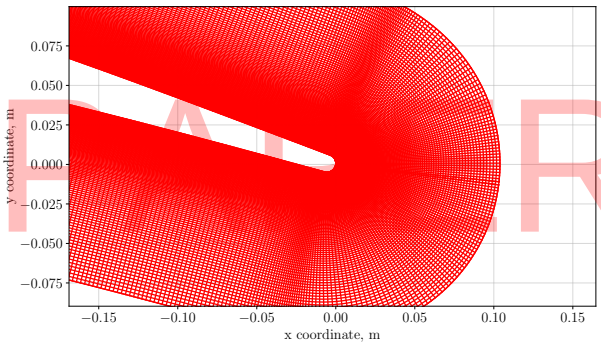

(c) Trailing edge meshing detail.

Fig. 1 DNS calculations mesh. Composed of two overlapping blocks: background and O-grid mesh.

The first block, which composes the background mesh, consists of 1800×1000 equidistant grid points along x and y directions respectively. The second block is an O-grid mesh that surrounds the airfoil (see Fig. 1b). This type of mesh allows controlling the refinement at the leading and trailing edges. In the present geometry, both leading and trailing edges are rounded with most of the points on the airfoil surface clustered in their neighbourhood, as seen in Fig. 1c. The O-grid mesh is composed of 1000×140 grid points in the tangential and normal directions to the airfoil. Overall, there are about 1.94M grid points in the x-y plane.

In the spanwise direction, a grid sensitivity has previously been evaluated [19]. The spanwise resolution in this study is such that 96 spectral modes are employed to discretize the 0.1c spanwise length, which was proven to be a sufficiently large spanwise extent [23]. With that, the whole domain is composed of around 190M cells. To provide an order of magnitude, once the flow is converged, around 72.5k CPU hours and 6k GPU hours have been employed to perform this simulation.

To ensure the stability of the computation, the non-dimensional time step is set to 1.5×10^{-5}, which is equivalent to a physical time step of 1.27×10^{-7} s. This time step provides a CFL < 1 in both meshing blocks. The resolution of the mesh is evaluated by means of the non dimensional grid sizes at the wall of the airfoil. The values in the wall-normal direction are $y^+ < 1$ for most of the airfoil surface, with $y^+_{\max} = 1.5$ at the leading edge. In the streamwise and spanwise directions, the normalized cell-wall distance are x^+ 20 and z^+ 25 respectively.

2. Initial and boundary conditions

To reproduce the experimental conditions of Ecole Centrale de Lyon or Université de Sherbrooke (UdeS), the installation effects have been considered. Such effects are produced by the jet influence, which modifies the airfoil loading [12]. A 2D RANS solution of the flow around the CD airfoil has been computed. In the simulation, the complete experimental geometric configuration is included, the domain configuration corresponds to the 'lips' configuration addressed in a previous work [9].

The turbulence model employed in the RANS calculation is the k-ω SST since it provides a good agreement with the experimental velocity fields. The steps followed to introduce the installation effects are the following ones [24]:

1) 2D RANS calculation initialization and run until convergence criteria are satisfied. The flow variables provide mean values that are used to initialize the flow field as well boundary conditions for the DNS computation.
2) Flow interpolation of the RANS case to the DNS 3D mesh. A polynomial interpolation is applied to the background mesh, whereas a nearest neighbour approach is the interpolating function for the O-grid region to prevent damping flow values near the wall [25]. The 2D flow field is extruded in the spanwise direction to cover the new 3D domain.
3) Extraction of inlet boundary conditions from the RANS solution. The velocity data at the limits of the domain are stored to be used as velocity profiles at the left and top boundaries. They provide the velocity profiles to be used at the inlets of the DNS domain.
4) The flow is initialized with open-jet installation effects by means of the interpolated data.
5) The calculations are performed in the time domain, imposing at every time step the mean velocity profiles at the inlet boundaries. This configuration will permit to test inlet turbulence injection, which will permit to observe the effects on the boundary layer evolution.

With that, the DNS accounts for the flow deflection effects shown in Fig. 2. Furthermore, as already mentioned, the DNS domain bounding box extension is sufficiently small to fit in the core of the jet in order to prevent introducing the effect of the shear layer produced by the wind tunnel 'lips' [10, 25].

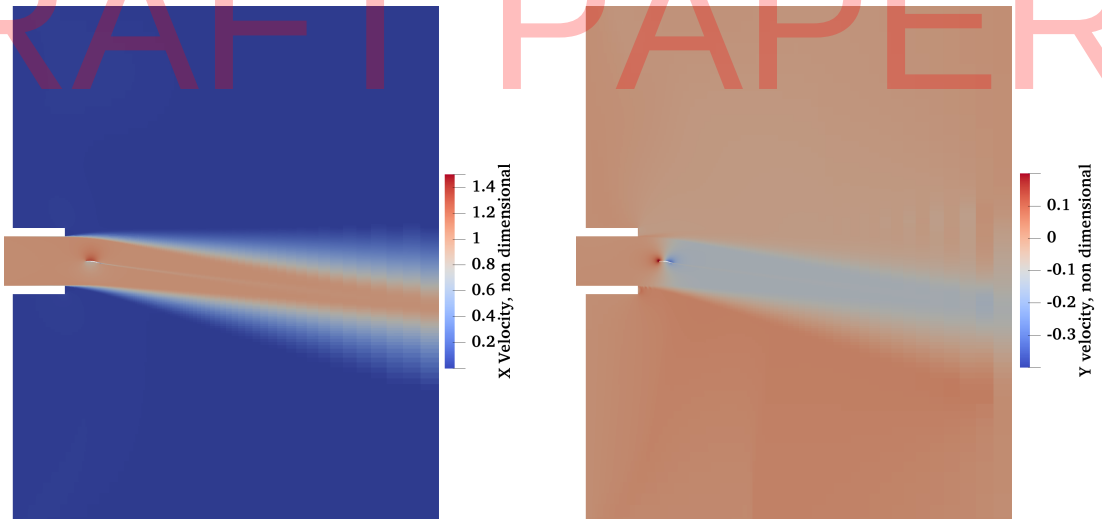

(a) x component of velocity. **(b) y component of velocity.**

Fig. 2 Velocity contours of the 2D RANS simulation employed as initialization values on DNS computation.

In the DNS computations, special attention has been paid to the boundaries of the domain to prevent spurious/nonphysical reflections. To damp the non-linear disturbances, a buffer region is included upstream of the physical domain with the aim of damping the flow perturbations before reaching the boundary and producing undesired reflecting waves. Downstream, a Zonal Characteristic Boundary Condition is applied [26] to ramp towards zero the flow perturbations before reaching the end of the domain. Finally, at the aerofoil surface, an adiabatic, no-slip condition is applied.

B. Acoustic-field model

To investigate the acoustic radiation from the CD airfoil, the DNS is coupled with an in-house Ffowcs Williams & Hawkings (FWH) solver named *SherFWH*. *SherFWH* is meant to compute the far-field acoustic pressure from near-field pressure provided by the DNS. The data that feeds the acoustic solver is recorded at a sampling frequency of 78.6 kHz. The FWH acoustic analogy requires to enclose the sound sources with a control surface, in this case the airfoil surface, so that the acoustic signature at any observer position is obtained from the following equation:

$$p'(\mathbf{x},t) = \underbrace{\frac{\partial}{\partial t}\int_{f=0}\left[\frac{Q_i n_i}{4\pi|\mathbf{x}-\mathbf{y}|}\right]_{\tau_e}\mathrm{d}S}_{\text{Thickness noise (monopole)}} - \underbrace{\frac{\partial}{\partial x_i}\int_{f=0}\left[\frac{L_{ij}n_j}{4\pi|\mathbf{x}-\mathbf{y}|}\right]_{\tau_e}\mathrm{d}S}_{\text{Loading noise (dipole)}} + \underbrace{\frac{\partial^2}{\partial x_i \partial x_j}\int_{f>0}\left[\frac{T_{ij}}{4\pi|\mathbf{x}-\mathbf{y}|}\right]_{\tau_e}\mathrm{d}V}_{\text{Source noise (quadrupole)}} \tag{8}$$

with the source terms Q_i, L_{ij}, T_{ij} the Lighthill's stress tensor and P_{ij} the compression tensor:

$$Q_i = \rho\left(u_i - v_i\right) + \rho_0 v_i \tag{9}$$

$$L_{ij} = \rho u_i\left(u_j - v_j\right) + P_{ij} \tag{10}$$

$$T_{ij} = \rho u_i u_j + \left[(p-p_0) - c_0^2(\rho-\rho_0)\right]\delta_{ij} - \sigma_{ij} \tag{11}$$

$$P_{ij} = (p-p_0)\,\delta_{ij} - \sigma_{ij} \tag{12}$$

The FWH formulation that is employed is the solid formulation, which requires the pressure fluctuations on the airfoil surface, where the resolution is the finest. In the solid formulation used here, two main terms compose the far-field acoustic pressure: the monopolar and the dipolar terms, which correspond to the thickness and loading noise respectively.

The location of the microphone arrays in the far field are such that both the distance to the trailing edge and the directivity can be evaluated. Fig. 3 provides a overview of the microphone locations. There are two categories of arrays, circumferential directivity and radial arrays.

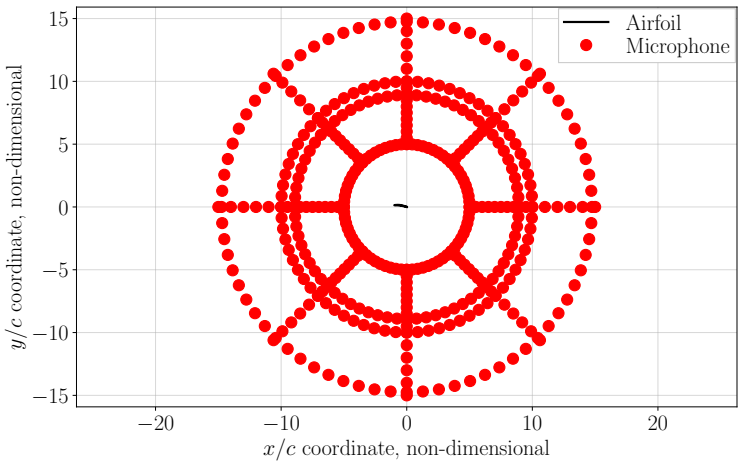

Fig. 3 Microphone locations used to compute pressure disturbances at several distances and angles from the trailing edge. Locations centered at the trailing edge.

Eight linear microphone arrays have been placed radially at every 45°. The microphones cover a distance of 5 to 15 chords from the trailing edge and are evenly distributed from 5 to 10 chords every 0.5 chord and from 10 to 15 chords

every chord. As for the directivity arrays, they are each composed of 72 microphones distributed every 5° over circles that are centred on the trailing edge. The distances from the trailing edge to arrays are 0.678, 1.21, 1.356 and 2 m.

III. Results

The wall-pressure distribution on the airfoil is used to evaluate the installation effects and measured at the sensor locations on the airfoil shown in Fig. 4. The chordwise and spanwise position of the sensors is collected in Tab. 1 [27].

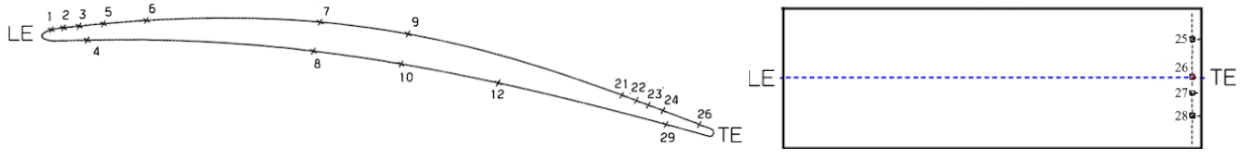

(a) Side view of the airfoil. **(b) Top view of the airfoil.**

Fig. 4 Pressure sensors location on the airfoil surface.

Table 1 Sensors location

Sensor	2	3	5	6	7	21	22	23	24	25	26	27	30
x/c	0.022	0.045	0.077	0.146	0.404	0.858	0.878	0.899	0.916	0.916	0.916	0.916	0.916
z/c	0.05	0.05	0.05	0.05	0.05	0.05	0.05	0.05	0.05	-0.0369	0.05	-0.0148	0.0369
	Leading edge to midchord					Trailing edge							

The wall-pressure coefficient is defined as:

$$C_p = \frac{p - p_0}{1/2\,\rho_0\,U_0^2} \tag{13}$$

where p_0, ρ_0 and U_0 are the reference free stream pressure, density and velocity respectively. The effect of the Laminar Separation Bubble (LSB) on the initial 10% of the chord at the suction side is more pronounced than in the experimental conditions because of the lack of upstream turbulence in the simulation, whereas in the experimental conditions, the turbulence intensity was about 0.8% at ECL, 0.4% at UdeS and 0.2% at TU-Delft. In general, there is a good agreement between experimental and numerical results, also compared to previous DNS studies by Wu [12].

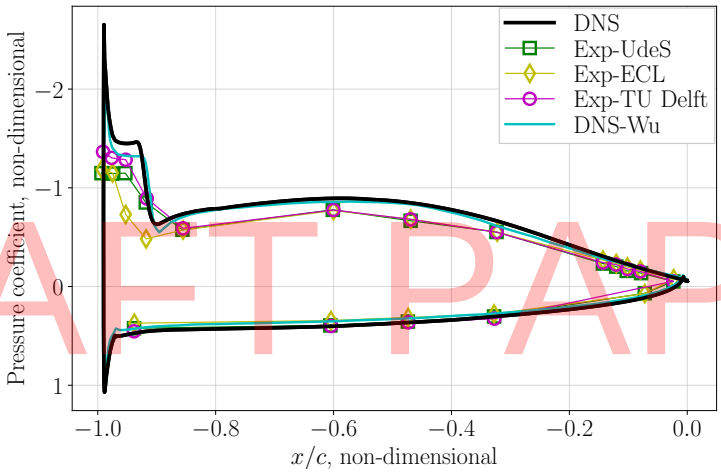

Fig. 5 Mean value of the pressure coefficient C_p, spanwise and temporal averaged.

The velocity profiles in the near wake have been compared to experimental and numerical data. The experimental data comes from MSU (Hot Wire, HW) and UdeS (Particle Image Velocimetry, PIV) [25]. Both, mean and fluctuating root mean square (RMS) velocities in the x and y directions are shown in Figs. 6 and 7 respectively. The locations to evaluate the near wake profiles are x/c =0.075, 0.169 and 0.206. Overall, the results of the velocity profiles show a good agreement with experimental data. At $x/c = 0.075$, the closest to the trailing edge, the profiles of the vertical velocity component v present a discrepancy of about 20% on the asymptotic external velocity (most likely related to the RANS uncertainty on the velocity profiles at the boundaries) which may imply a modification in the airfoil loading. However, when moving farther downstream, the vertical velocity component of the region unaffected by the wake matches the experimental data. Furthermore, the peak velocity on the midline of the wake deficit match the experimental data well ($y/c \approx -0.02$).

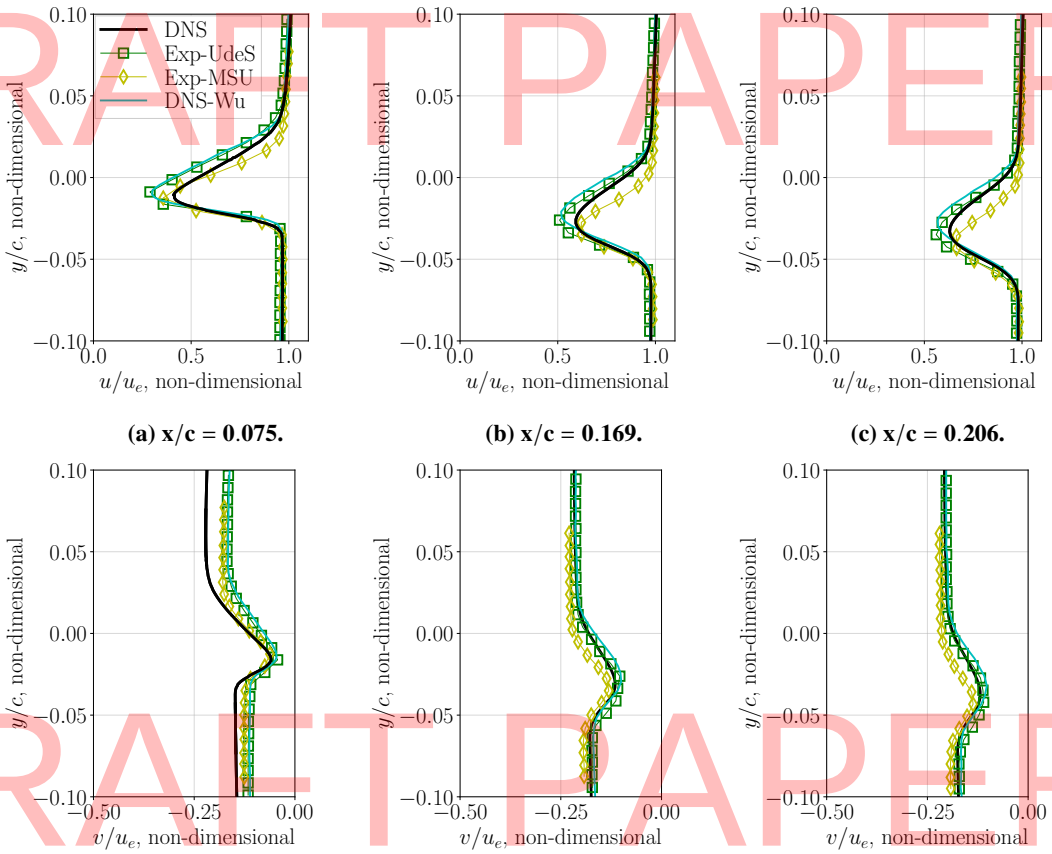

(a) x/c = 0.075. **(b) x/c = 0.169.** **(c) x/c = 0.206.**

(d) x/c = 0.075. **(e) x/c = 0.169.** **(f) x/c = 0.206.**

Fig. 6 Near wake velocity profiles. Comparison with experimental and DNS data extracted from Wu *et al.* [12].

The RMS of the fluctuating velocity profiles show a good overall agreement particularly with the HW measurements. There is some reduction of the peak amplitudes in the wake deficit (see Fig. 7), which might be caused by some smoothing introduced by the spatial interpolation, as a result of moving from the most refined mesh in the O-grid region towards the background mesh. Nevertheless, the results show that the present DNS computation provides a quite reliable hydrodynamic field that may lead to a proper representation of the acoustic field.

To investigate the acoustic radiation from the airfoil to the far-field, the DNS results are coupled with an acoustic solver *SherFWH*. It yields the acoustic far field from near field data, in particular, the wall-pressure fluctuations. In this case, the solid formulation is used to obtain the far field. An analysis of the coherence of the wall-pressure statistics is then carried out to assess the reliability of the DNS computations.

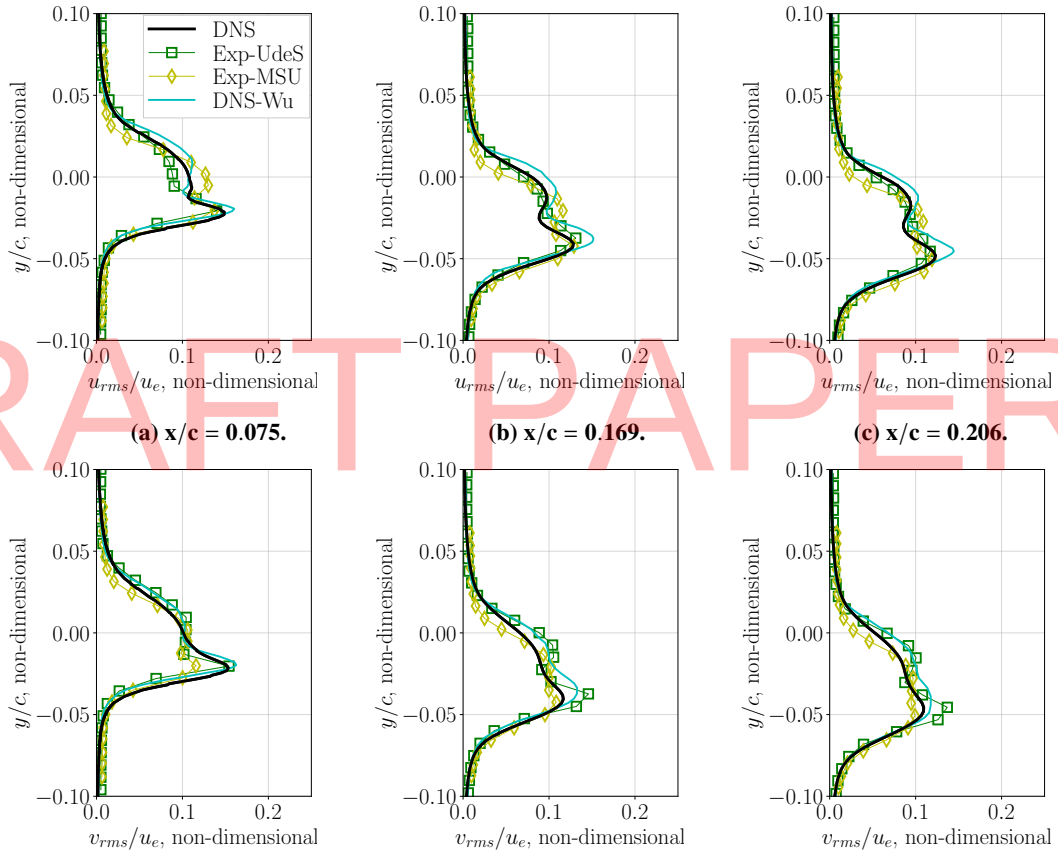

(a) x/c = 0.075. **(b) x/c = 0.169.** **(c) x/c = 0.206.**

(d) x/c = 0.075. **(e) x/c = 0.169.** **(f) x/c = 0.206.**

Fig. 7 Near wake fluctuating velocity profiles. Comparison with experimental and DNS data extracted from Wu *et al.* [12].

The coherence is defined as follows[28]:

$$\gamma^2(\boldsymbol{\xi},\omega) = \frac{\left|\Psi_{pp}(\boldsymbol{\xi},\omega)\right|^2}{\phi_{pp}(\omega)^2} \tag{14}$$

where $\Psi_{pp}(\boldsymbol{\xi},\omega)$ is the cross spectrum. It provides the level of correlation between two points which are spatially separated at a given frequency. This separation might be a given streamwise distance ξ_x or spanwise distance ξ_z.

The streamwise coherence is represented in Fig.8. Fig. 8a stands for the sensor locations near the leading edge, whereas Fig. 8b provides the sensors located near the trailing edge. The data is compared with the ECL experiment. Near the leading edge, the reference sensor from which the coherence is computed is sensor 5. At low frequencies, sensor 2 shows the highest values of coherence with sensor 5, whereas the rest of the sensors have almost no correlation. A priori, since sensors 3 and 6 are located closer to sensor 5 than the others, their coherence should be of the same order or even larger than sensor 2. At high frequencies, around 4 kHz, there appears a hump in sensors 3 and 6. This hump might be related to the vortex shedding caused by the laminar flow separation. The experimental results show two trends. At low frequencies (up to 1 kHz) there is an exponential decay in sensors 2, 3, and 6, and almost null coherence in the locations that are farther from sensor 5. Then, the hump at high frequencies appears. This time, it is centered at about 1 kHz. The DNS results into a shift towards the high frequencies in the effect of the LSB vortex shedding.

The evaluation of the coherence near the trailing edge shows the decreasing trend of the coherence with the increase in distance between the sensors. Two main humps appear, one centered around 200 Hz and another centered around 700 Hz. The experimental data exhibits once again the exponential decaying trend up to 1 kHz and a small bump of correlated structures around 1 kHz. Moreau & Roger [16] claimed a sort of vortex shedding similar to the one due to the laminar flow separation at the leading edge to be the source of such a bump. The spanwise coherence has been

evaluated close to the trailing edge (98% of the chord). The spanwise coherence is represented versus the frequency in Fig. 9. The spanwise coherence is affected mainly at low frequencies, as noted by Wang *et al.* [29]. As expected in turbulent boundary layers, as the distance between the sensors 25, 27 and 30 increases with respect to sensor 26, from which the coherence has been computed, the spanwise coherence is lower. In the current DNS, the amplitude of the spanwise coherence is similar to experiment [16], but it presents larger fluctuations around 1 kHz, which does not yield the clear exponential decay seen in the experimental data [16] similar to the Corcos model [30] for a fully developed boundary layer over a flat plate.

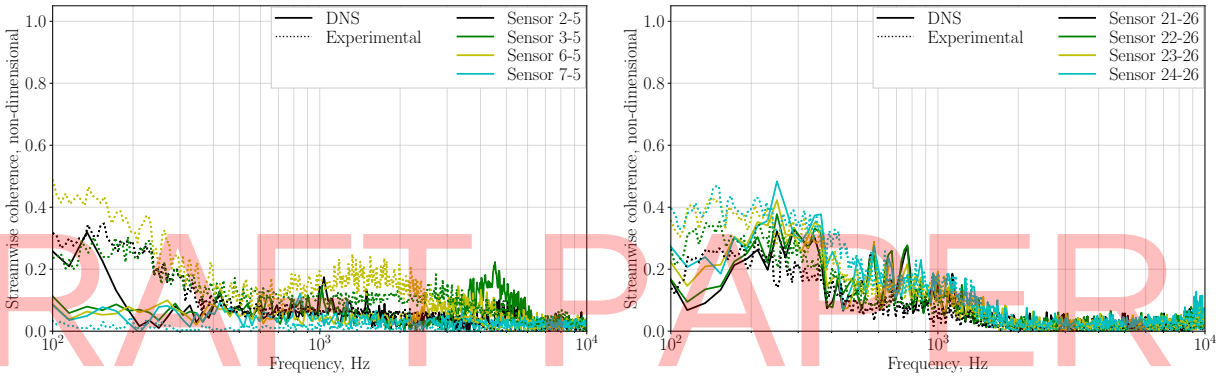

(a) Front of the CD airfoil. **(b) Aft of the CD airfoil.**

Fig. 8 Streamwise coherence at the front and aft positions on the suction side, with sensors 5 and 26 as reference respectively. Comparison with experimental data extracted from Moreau & Roger [16].

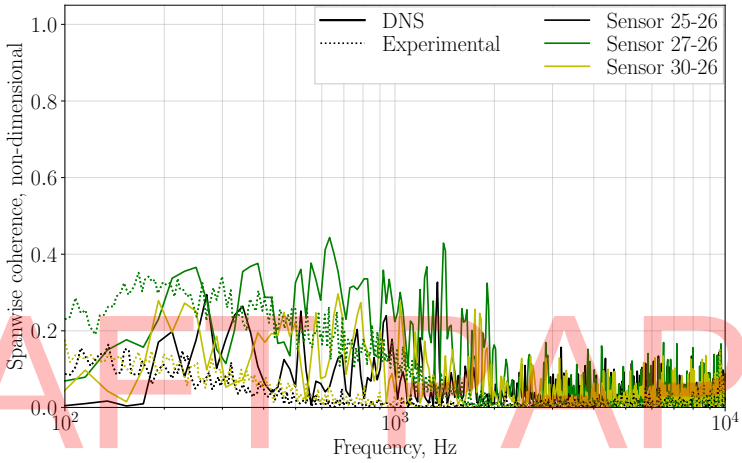

Fig. 9 Spanwise coherence close to the trailing edge. Comparison with experimental data extracted from Moreau & Roger [16].

Fig. 10 shows the results of the predicted far field Sound Pressure Levels for four of the eight line microphone arrays. As the distance from the trailing edge is increased, the sound levels decrease progressively. The wake of the airfoil, which is aligned with the airfoil slope, as displayed in Fig. 10, produces an effect on the SPL at frequencies above 10 kHz. Notice that in the contours of the dilatation field (Fig. 12c), an instability source appears in the near wake, close to the trailing edge. It could drive the oscillating effect characterized by important peaks and valleys at high frequencies found in the microphone array located at 0° (Fig. 10a). This behaviour is characteristic of interference patterns. This effect is still noticeable at 315° (-45°, Fig. 10b). When moving away from the wake, the repercussion on the sound levels is less pronounced, at 90° the effect of the wake at high frequencies is undetectable.

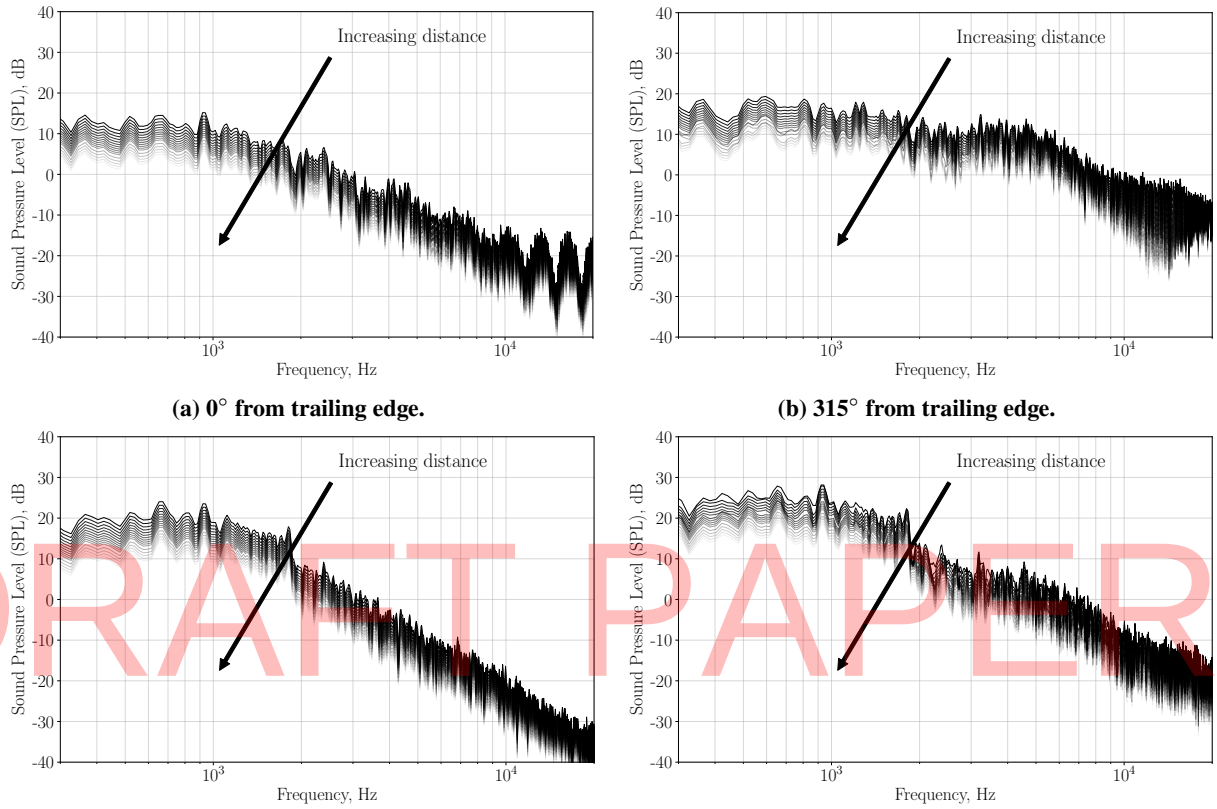

(a) 0° from trailing edge. **(b) 315° from trailing edge.**

(c) 270° from trailing edge. **(d) 90° from trailing edge.**

Fig. 10 Sound Pressure Levels at different angles and distances from the airfoil trailing edge. As the solidity of the lines decreases, the distance is increased.

The noise spectrum 2 m away from the trailing edge at 90° to the flow direction is shown in Fig. 11. The predicted data is compared with experimental data and numerical data. The sound pressure levels from Wu *et al.* [12] are computed by means of the FWH solid formulation. The noise prediction shows a good agreement with experimental data at low to medium frequencies. Nonetheless, the current DNS result presents a drop at high frequencies instead of the plateau that was obtained in UdeS and previous DNS cases. The source in the near wake evidenced in the dilatation contours in Fig. 12 is not included in the solid formulation of the FWH analogy, and might be responsible for the drop at high frequencies that is not seen experimentally.

In Fig. 12 the instantaneous contours of the Q-criterion colored by the velocity magnitude superimposed to the dilatation contours are shown. The dilatation field is computed as $-\partial\rho/\partial t$ since it does not depend on the spatial discretization but only on the temporal resolution. The dilatation contours show the noise sources near the airfoil. There appear three main noise sources: the laminar separation bubble, the flow detachment/reattachment over the airfoil surface, which leads into trailing edge noise and a third source right downstream the trailing edge. The bandpass filtering that has been introduced in the dilatation field aims to determine the frequency contribution of the different noise sources.

At low frequencies, the main contribution to the noise is the trailing edge, with the additional low effect of the turbulent flow passing through the suction side. At high frequencies, the main noise source is located around the laminar separation bubble, as a result of the laminar flow initial breakdown [31]. Also, the effect of the wake source is seen, even though it is not as relevant as the LSB effect. When looking at the non-filtered dilatation field, it is the composition of all the noise sources. The combination of the trailing edge source together with the near wake makes the rear airfoil region a critical noise emission area, the noise emission source lays in between the trailing edge noise source found at low frequencies and the near wake source found at high frequencies.

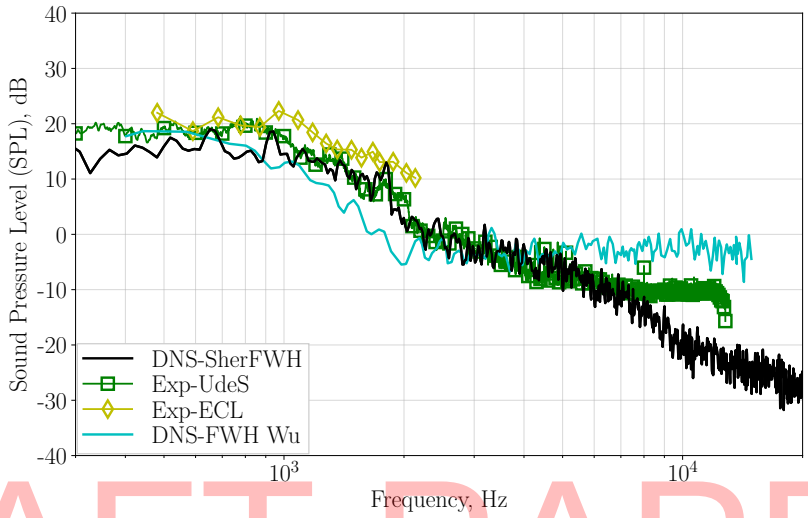

Fig. 11 Sound Pressure Levels perpendicular to the trailing edge at 2 m distance. Data compared to experimental and numerical data available.

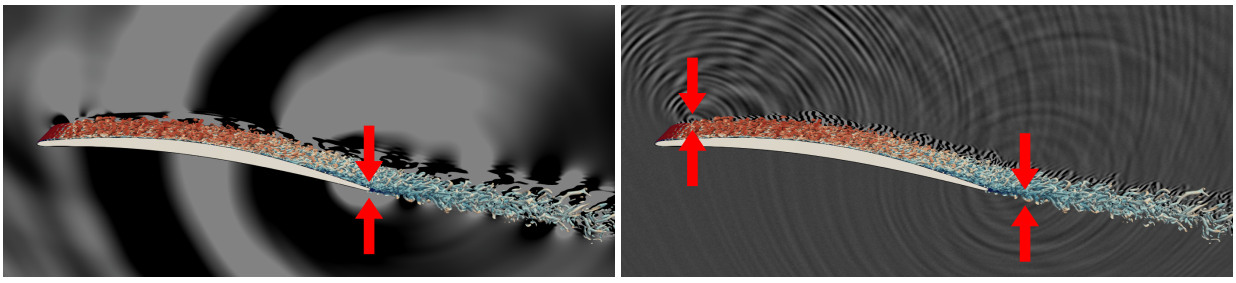

(a) Low frequencies filtering (10-1000 Hz).

(b) High frequencies filtering (4-5 kHz).

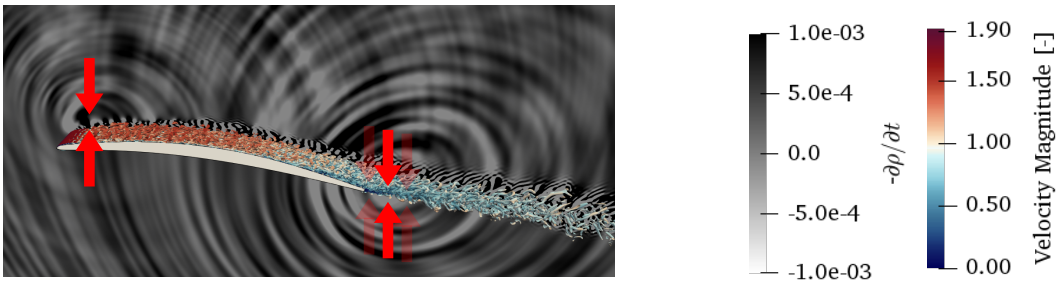

(c) No frequency filtering.

Fig. 12 Instantaneous field of Q-criterion velocity magnitude superimposed to the dilatation field contours $-\partial\rho/\partial t$ Filtering at various frequency ranges.

Finally, the single-frequency directivity is shown in Fig. 13. For low frequencies (Helmholtz number $kc < 1$, with $k = 2\pi f/c_0$ the acoustic wave number, f the frequency and c_0 the speed of sound in the surrounding medium) the directivity shows a dipolar distribution with its characteristic symmetrical lobe pattern. As the frequency increases, the source become non compact and the effect of quadrupolar sources becomes more and more important. Extra lobes appear and the tilting of the directivity pattern is aligned to the incoming flow direction. The noise propagation gets a preferential direction towards the flow downstream, which is linked to the effect of the sources around the leading edge. The coherence of the LSB and the laminar boundary layer seen in Fig. 8a indicates that this interaction may produce the reduction on noise levels at the leading edge for all frequency content.

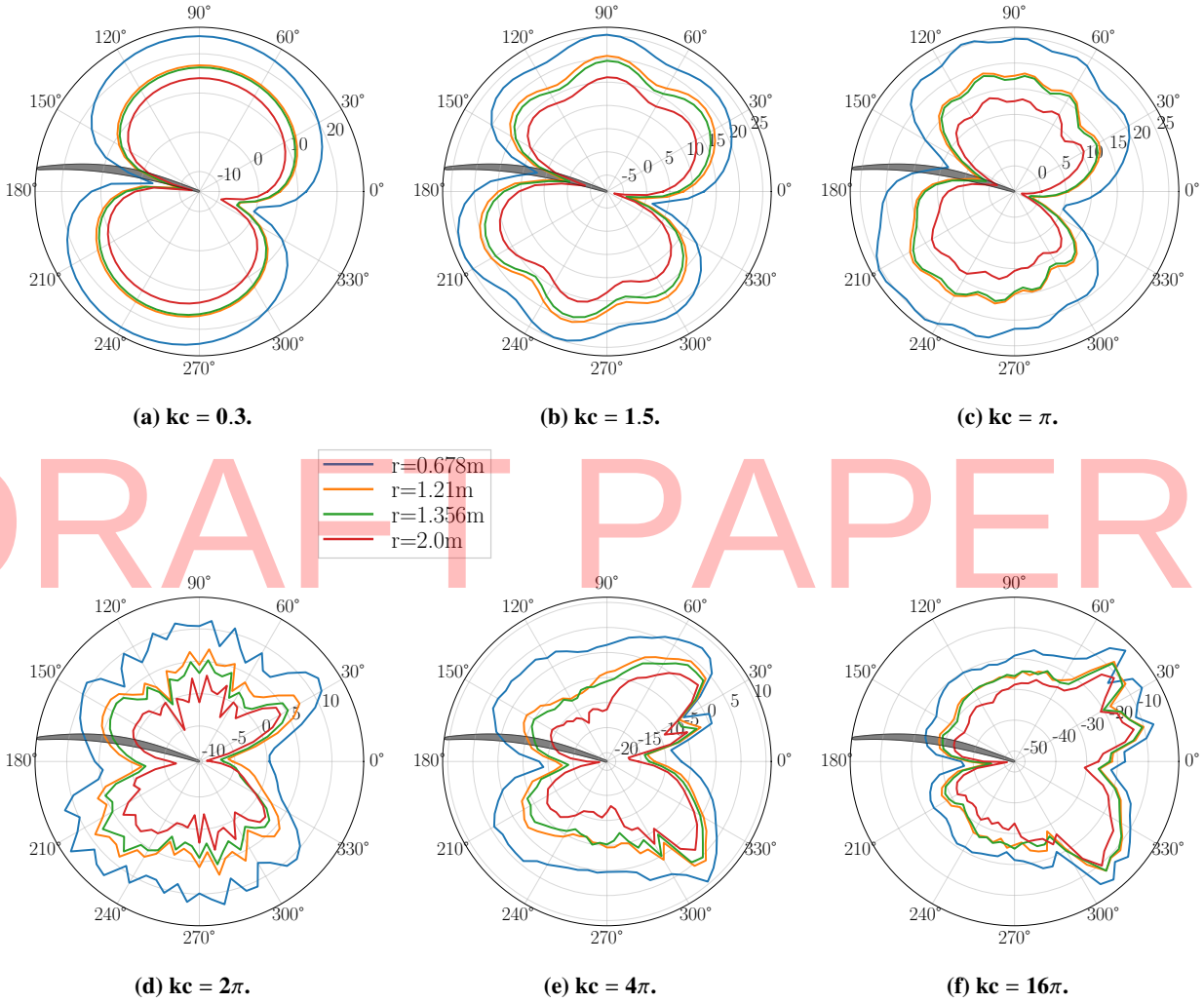

(a) kc = 0.3. **(b) kc = 1.5.** **(c) kc = π.**

(d) kc = 2π. **(e) kc = 4π.** **(f) kc = 16π.**

Fig. 13 Single-frequency directivity on far field at several distances from the trailing edge. Sound Pressure Level (SPL), dB.

IV. Conclusion

The flow over a Controlled-Diffusion airfoil at a geometric angle of attack of 8°, a chord-based Reynolds number of $Re_c = 1.5 \times 10^5$ and free-stream Mach number of $M = 0.25$ has been carried out by means of compressible DNS. The aim of this research is to study the relationship between the near and far field acoustics and how they relate to noise generation mechanisms.

The numerical computations have been validated by means of experimental data. The numerical simulations include the installation effects as they can be found out in the experimental facilities of ECL, UdeS and MSU. The aerodynamic data –pressure coefficient and mean and fluctuating velocity profiles– show good agreement with the available experimental data. The laminar separation bubble observed in the simulations is larger than the one obtained experimentally because in the simulation there is no inlet turbulence injection. At the closest point of the trailing edge, the vertical velocity profile shows a slight deviation from experiments in the region unaffected by the velocity deficit.

Three main noise sources have been found in the simulations, and they have been evidenced by means of filtered dilatation contours:

- Flow separation and reattachment at the leading edge on the airfoil suction side. This effect produces the laminar separation bubble.
- Interaction between the turbulent flow and the airfoil suction side, which reaches up to the trailing edge.
- A noise source in the near wake, located close to the trailing edge.

The coherence in the streamwise and spanwise directions has been evaluated. The streamwise coherence near the leading edge shows a shift of coherence bumps towards higher frequencies compared to experimental data sign of a different LSB. Very good agreement is achieved near the trailing edge, stressing that the mean convection velocity of turbulent structures is locally well predicted. In the spanwise direction, the levels are well predicted, even though the low frequency range evidences the need of running the simulation for a longer time to capture the low frequency content properly.

In order to predict the far field noise, the solid formulation of the FWH acoustic analogy has been employed. This formulation uses the pressure fluctuations at the wall to propagate the pressure field far from the airfoil. The sound pressure levels evaluated at a distance of 2 m perpendicular to the trailing edge agree with experimental data up to around 5 kHz. For higher frequencies, there is a decay on the sound pressure levels which might be due to the near wake source that has not been included in the FWH solid formulation. The sound pressure level directivity plots evolve from a dipolar distribution aligned with the airfoil towards patterns with multiple lobes with downstream preference propagation direction as the frequency is increased caused by an increasing leading-edge noise contribution (LSB).

V. Acknowledgement

This work was partly supported by the French "Programme d'Investissements d'avenir" EUR-TSAE. We also acknowledge the support of the Natural Sciences and Engineering Research Council of Canada (NSERC) through the Discovery grant. This research was undertaken with the assistance of resources and services from the Digital Research Alliance of Canada and the National Computational Infrastructure (NCI), which is supported by the Australian Government.

References

[1] Ffowcs-Williams, J. E., and Hall, L. H., "Aerodynamic sound generation by turbulent flow in the vicinity of a scattering half plane," *Journal of Fluid Mechanics*, Vol. 40, No. 4, 1970, pp. 657–670. https://doi.org/10.1017/S0022112070000368.

[2] Amiet, R. K., "Noise due to turbulent flow past a trailing edge," *Journal of Sound and Vibration*, Vol. 47, No. 3, 1976, pp. 387–393. https://doi.org/10.1016/0022-460X(76)90948-2.

[3] Howe, M. S., *Theory of Vortex Sound*, Cambridge University Press, 2003.

[4] Boukharfane, R., Bridel-Bertomeu, T., Bodart, J., Joly, L., and Jacob, M. C., "Characterization of the pressure fluctuations within a controlled-diffusion airfoil boundary layer at large Reynolds numbers," *25th AIAA/CEAS Aeroacoustics Conference*, 2019, pp. 20–23. https://doi.org/10.2514/6.2019-2722.

[5] Boukharfane, R., Parsani, M., and Bodart, J., "Characterization of pressure fluctuations within a controlled-diffusion blade boundary layer using the equilibrium wall-modelled LES," *Scientific Reports*, Vol. 10, No. 1, 2020, pp. 1–19. https://doi.org/10.1038/s41598-020-69671-y.

[6] Deuse, M., and Sandberg, R. D., "Different noise generation mechanisms of a controlled diffusion aerofoil and their dependence on Mach number," *Journal of Sound and Vibration*, Vol. 476, 2020, p. 115317. https://doi.org/10.1016/j.jsv.2020.115317.

[7] Sandberg, R. D., Sandham, N. D., and Joseph, P. F., "Direct numerical simulations of trailing-edge noise generated by boundary-layer instabilities," *Journal of Sound and Vibration*, Vol. 304, No. 3, 2007, pp. 677–690. https://doi.org/10.1016/j.jsv.2007.03.011.

[8] Sandberg, R. D., and Sandham, N. D., "Direct numerical simulation of turbulent flow past a trailing edge and the associated noise generation," *Journal of Fluid Mechanics*, Vol. 596, 2008, p. 353–385. https://doi.org/10.1017/S0022112007009561.

[9] Sanjosé, M., Moreau, S., Kim, M. S., and Pérot, F., "Direct self-noise simulation of the installed Controlled Diffusion airfoil," *American Institute of Aeronautics and Astronautics*, 2011. https://doi.org/10.2514/6.2011-2716, 17th AIAA/CEAS Aeroacoustics Conference(32nd AIAA Aeroacoustics Conference).

[10] Winkler., J., Wu, H., Moreau, S., Carolus, T., and Sandberg, R., "Trailing-edge broadband noise prediction of an airfoil with boundary-layer tripping," *Journal of Sound and Vibration*, Vol. 482, 2020, pp. 115450:1–25.

[11] Wu, H., Moreau, S., and Sandberg, R., "Effects of pressure gradient on the evolution of velocity-gradient tensor invariant dynamics on a controlled-diffusion aerofoil at $Re_c = 150000$," *Journal of Fluid Mechanics*, Vol. 868, 2019, pp. 584–610.

[12] Wu, H., Moreau, S., and Sandberg, R., "On the noise generated by a controlled-diffusion aerofoil at $Re_c = 1.5 \times 10^5$," *Journal of Sound and Vibration*, Vol. 506, 2020, pp. 116152: 1–20. https://doi.org/10.1017/jfm.2019.129.

[13] Wu, H., Sandberg, R., and Moreau, S., "Stability characteristics of different aerofoil flows at $Re_c = 1.5\times10^5$ and the implications for aerofoil self-noise," *Journal of Sound and Vibration*, Vol. 487, 2021, pp. 115620: 1–25. https://doi.org/10.1017/jfm.2019.129.

[14] Jones, L. E., Sandham, N. D., and Sandberg, R. D., "Acoustic source identification for transitional airfoil flows using cross correlations," *American Institute of Aeronautics and Astronautics*, Vol. 48, 2010, pp. 2299–2312. https://doi.org/10.2514/1.J050345.

[15] Moreau, S., Henner, M., Iaccarino, G., Wang, M., and Roger, M., "Analysis of Flow Conditions in Freejet Experiments for Studying Airfoil Self-Noise," *American Institute of Aeronautics and Astronautics*, Vol. 41, No. 10, 2003, pp. 1895–1905. https://doi.org/10.2514/2.1905.

[16] Moreau, S., and Roger, M., "Effect of Airfoil Aerodynamic Loading on Trailing-Edge Noise Sources," *American Institute of Aeronautics and Astronautics*, Vol. 43, No. 1, 2005, pp. 41–52. https://doi.org/10.2514/1.5578.

[17] Moreau, S., Iaccarino, G., Kang, S., Khalighi, Y., and Wang, M., "Numerical simulation of a low speed fan blade," *Proceedings of the CTR Summer Program*, 2004, p. 195 – 207. URL https://www.scopus.com/inward/record.uri?eid=2-s2.0-43449088721&partnerID=40&md5=1f9b61719d30ca2a32217df090a4b31d.

[18] Sanjosé, M., Moreau, S., Kim, M.-S., and Pérot, F., "Direct self-noise simulation of the installed Controlled Diffusion airfoil," *American Institute of Aeronautics and Astronautics*, 2011. https://doi.org/10.2514/6.2011-2716, 2011 AIAA/CEAS Aeroacoustics Conference.

[19] Arroyo Ramo, A., Moreau, S., Sandberg, R. D., Bauerheim, M., and Jacob, M. C., "Direct Numerical Simulation of Controlled Diffusion airfoil," *28th AIAA/CEAS Aeroacoustics Conference*, 2022, pp. 1–22. https://doi.org/10.2514/6.2022-2815.

[20] Sandberg, R. D., "Compressible-Flow DNS with Application to Airfoil Noise," *Flow Turbulence Combust*, Vol. 95, 2015, pp. 211–229. https://doi.org/10.1007/s10494-015-9617-1.

[21] Carpenter, M. H., Gottlieb, D., and Abarnanel, S., "Stable and accurate boundary treatments for compact, high-order finite-difference schemes," *Applied Numerical Mathematics*, Vol. 12, 1993, pp. 55–87. https://doi.org/10.1006/jcph.1993.1182.

[22] Deuse, M., and Sandberg, R. D., "Implementation of a stable high-order overset grid method for high-fidelity simulations," *Computers & Fluids*, Vol. 211, 2020, p. 104449.

[23] Wang, M., and Moin, P., "Computation of trailing-edge flow and noise using large-eddy simulation," *American Institute of Aeronautics and Astronautics*, Vol. 38, 2000, pp. 2201–2209. https://doi.org/10.2514/2.895.

[24] Lee, S., Ayton, L., Bertagnolio, F., Moreau, S., Chong, T. P., and Joseph, P., "Turbulent boundary layer trailing-edge noise: Theory, computation, experiment, and application," *Progress in Aerospace Sciences*, Vol. 126, No. June, 2021, p. 100737. https://doi.org/10.1016/j.paerosci.2021.100737, URL https://doi.org/10.1016/j.paerosci.2021.100737.

[25] Wu, H., "Direct Numerical Simulation of Airfoil Self-Noise at High Reynolds Numbers," Ph.D. thesis, Université de Sherbrooke, 2019. Department of Mechanical Engineering.

[26] Sandberg, R. D., and Sandham, N. D., "Nonreflecting Zonal Characteristic Boundary Condition for Direct Numerical Simulation of Aerodynamic Sound," *American Institute of Aeronautics and Astronautics*, Vol. 44, No. 2, 2006, pp. 402–405. https://doi.org/10.2514/1.19169.

[27] Höwer, D., "Unsteady pressure fluctuations on the surface of a Controlled Diffusion airfoil," Master's thesis, RWTH University, 2012.

[28] Caiazzo, A., Pargal, S., Wu, H., Sanjosé, M., Yuan, J., and Moreau, S., "On the effect of adverse pressure gradients on wall-pressure statistics in a controlled-diffusion aerofoil turbulent boundary layer," *Journal of Fluid Mechanics*, Vol. 960, 2023, p. A17. https://doi.org/10.1017/jfm.2023.157.

[29] Wang, M., Moreau, S., Iaccarino, G., and Roger, M., "LES prediction of wall-pressure fluctuations and noise of a low-speed airfoil," *International Journal of Aeroacoustics*, Vol. 8, No. 3, 2009, pp. 177–198. https://doi.org/10.1121/1.2934513.

[30] Corcos, G. M., "The structure of the turbulent pressure field in boundary-layer flows," *Journal of Fluid Mechanics*, Vol. 18, No. 3, 1964, p. 353–378. https://doi.org/10.1017/S002211206400026X.

[31] Greschner, B., Grilliat, J., Jacob, M. C., and Thiele, F., "Measurements and wall Modeled LES Simulation of Trailing Edge Noise Caused by a Turbulent Boundary Layer," *International Journal of Aeroacoustics*, Vol. 9, No. 3, 2010, pp. 329–355. https://doi.org/10.1260/1475-472X.9.3.329, URL https://doi.org/10.1260/1475-472X.9.3.329.

DRAFT PAPER